



Vibrational dynamics of the type-I clathrates $A8Sn_{44}2$ ($A = Cs, Rb, K$) from lattice-dynamics calculations, inelastic neutron scattering, and specific heat measurements

Christophe Candolfi, Michael Marek Koza, Umut Aydemir, Wilder Carrillo-Cabrera, Yuri Grin, Franck Steglich, Michael Baitinger

► To cite this version:

Christophe Candolfi, Michael Marek Koza, Umut Aydemir, Wilder Carrillo-Cabrera, Yuri Grin, et al.. Vibrational dynamics of the type-I clathrates $A8Sn_{44}2$ ($A = Cs, Rb, K$) from lattice-dynamics calculations, inelastic neutron scattering, and specific heat measurements. *Journal of Applied Physics*, 2020, 127 (14), pp.145104. 10.1063/1.5117217 . hal-03997338

HAL Id: hal-03997338

<https://hal.science/hal-03997338>

Submitted on 20 Feb 2023








HAL is a multi-disciplinary open access archive for the deposit and dissemination of scientific research documents, whether they are published or not. The documents may come from teaching and research institutions in France or abroad, or from public or private research centers.

L'archive ouverte pluridisciplinaire **HAL**, est destinée au dépôt et à la diffusion de documents scientifiques de niveau recherche, publiés ou non, émanant des établissements d'enseignement et de recherche français ou étrangers, des laboratoires publics ou privés.

Vibrational dynamics of the type-I clathrates $A_8\text{Sn}_{44}\square_2$ ($A = \text{Cs}, \text{Rb}, \text{K}$) from lattice-dynamics calculations, inelastic neutron scattering, and specific heat measurements

Cite as: J. Appl. Phys. 127, 145104 (2020); <https://doi.org/10.1063/1.5117217>

Submitted: 29 June 2019 . Accepted: 28 March 2020 . Published Online: 14 April 2020

C. Candolfi , M. M. Koza , U. Aydemir , W. Carrillo-Cabrera , Yu. Grin , F. Steglich , and M. Baitinger 



View Online



Export Citation



CrossMark

HIDEN
ANALYTICAL

Instruments for Advanced Science

Contact Hiden Analytical for further details:

W www.HidenAnalytical.com
E info@hiden.co.uk

[CLICK TO VIEW](#) our product catalogue

Gas Analysis

- dynamic measurement of reaction gas streams
- catalysis and thermal analysis
- molecular beam studies
- dissolved species probes
- fermentation, environmental and ecological studies

Surface Science

- UHV TPD
- SIMS
- end point detection in ion beam etch
- elemental imaging - surface mapping

Plasma Diagnostics

- plasma source characterization
- etch and deposition process reaction kinetic studies
- analysis of neutral and radical species

Vacuum Analysis

- partial pressure measurement and control of process gases
- reactive sputter process control
- vacuum diagnostics
- vacuum coating process monitoring

Vibrational dynamics of the type-I clathrates $A_8\text{Sn}_{44}\square_2$ ($A = \text{Cs}, \text{Rb}, \text{K}$) from lattice-dynamics calculations, inelastic neutron scattering, and specific heat measurements

Cite as: J. Appl. Phys. 127, 145104 (2020); doi: 10.1063/1.5117217

Submitted: 29 June 2019 · Accepted: 28 March 2020 ·

Published Online: 14 April 2020



View Online



Export Citation



CrossMark

C. Candolfi,^{1,2,a)} M. M. Koza,³ U. Aydemir,^{4,5} W. Carrillo-Cabrera,² Yu. Grin,² F. Steglich,² and M. Baitinger²

AFFILIATIONS

¹Institut Jean Lamour, UMR 7198 CNRS-Université de Lorraine, 2 allée André Guinier- Campus ARTEM, BP 50840, 54011 Nancy Cedex, France

²Max-Planck-Institut für Chemische Physik fester Stoffe, Nöthnitzer Str. 40, 01187 Dresden, Germany

³Institut Laue Langevin, 6 Rue Jules Horowitz, B.P. 156, 38042 Grenoble Cedex 9, France

⁴Department of Chemistry, Koç University, Rumelifeneri Yolu, Sariyer, Istanbul-34450, Turkey

⁵Koç University Boron and Advanced Materials Application and Research Center, Rumelifeneri Yolu, Sariyer, Istanbul-34450, Turkey

Note: This paper is part of the special topic on Advanced Thermoelectrics.

a) Author to whom correspondence should be addressed: christophe.candolfi@univ-lorraine.fr

ABSTRACT

We report on a joint theoretical and experimental study of the vibrational dynamics of the type-I clathrates $A_8\text{Sn}_{44}\square_2$ ($A = \text{K}, \text{Rb}, \text{Cs}$, and \square stands for a vacancy) by high-resolution inelastic neutron scattering experiments combined with low-temperature specific heat measurements (2–300 K). *Ab initio* lattice dynamics calculations were performed on hypothetical vacancy-free $A_8\text{Sn}_{46}$ clathrates in order to determine the phonon dispersions and vibrational density of states $Z(\omega)$. The temperature dependence of the generalized vibrational density of states (GVDOS) was traced from 420 K down to 50 K, paying particular attention to the low-energy region of the GVDOS spectra. In the Cs and Rb compounds, the inelastic signal at low energies is dominated by several peaks mainly associated with the dynamics of the alkali metal atoms A in the polyhedral cages of the clathrate structure. In contrast, the low-energy spectrum of the K compound features a more pronounced contribution of the weighed modes of the framework Sn atoms. Upon cooling, the A -weighted modes soften regardless of the nature of the alkali element. The shift observed is similar for the three compounds and of small amplitude, suggestive of a dominant quasi-harmonic behavior above 50 K. The distinct dynamics of the K atoms in comparison to Cs and Rb is further demonstrated by the analyses of the low-temperature specific heat data, indicating that the low-energy Sn-weighted modes cannot be described by a Debye model with Einstein-like contributions.

Published under license by AIP Publishing. <https://doi.org/10.1063/1.5117217>

I. INTRODUCTION

Understanding the underlying physical mechanisms responsible for the glass-like thermal conductivity (κ) exhibited by some crystalline materials has attracted considerable attention over the last few decades for both fundamental and practical reasons. Such unusual behavior has been observed in natural minerals,^{1–4} complex crystal structures with a large number of atoms per unit cell,^{5–12} and cage-

like compounds,^{13–21} with the type-I clathrates being one of the most prominent examples.²² The crystal structure of these materials is composed of covalently bonded frameworks in the large cavities of which “guest” atoms reside [polyhedral cages; Fig. 1(a)].^{23,24} Their vibrational dynamics is associated with low-energy, non-dispersive optical phonons that hybridize with the host lattice and efficiently disrupt the propagation of acoustic phonons. These low-energy modes tend to favor three-phonon processes, thereby reducing the

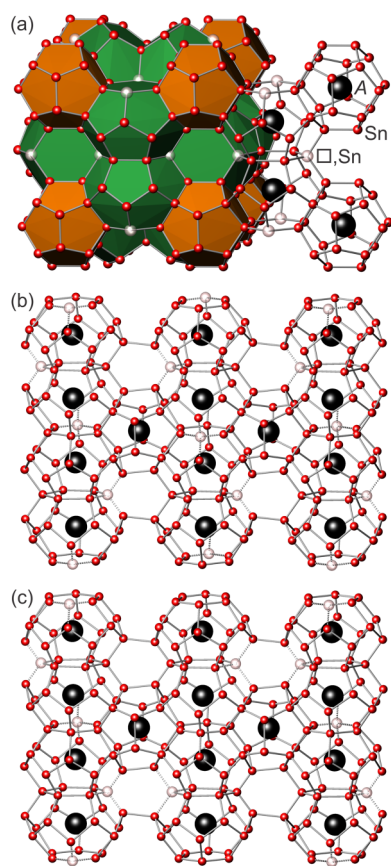


FIG. 1. (a) The crystal structure of type-I clathrates $A_8\text{Sn}_{44}\square_2$ with 20-atom (orange) and 24-atom (green) polyhedra within the 3D-framework centered by guest atoms A1 and A2, respectively. In this figure, the different Sn sites that form the polyhedral cages are not distinguished. (b) Spiral arrangement of vacancies (\square) in $2a \times 2a \times 2a$ superstructure. (c) Vacancies forming pairs in the basal plane in a tetragonal superstructure ($2a \times 2a \times 2c$).

acoustic phonon lifetime and hence, κ .^{18,25–34} Recent measurements of the phonon lifetimes in the type-I clathrate $\text{Ba}_8\text{Au}_{5.33}\text{Ge}_{40.67}$ evidenced unexpectedly long acoustic phonon lifetimes corresponding to phonon mean free paths on the order of a few tens of nanometers.³⁵ In addition to the phonon filter effect that has been shown to reduce the phonon transport and to control the position of the low-temperature peak in κ in type-I clathrates,^{26,27} the partial breaking of translational symmetry by non-periodic Ge-by-Au substitution and local structural distortions observed in $\text{Ba}_{7.81}\text{Ge}_{40.67}\text{Au}_{5.33}$ may also play a role in the thermal transport.^{35–37}

Several experimental probes such as Raman spectroscopy, extended x-ray absorption fine structure (EXAFS), ultrasonic attenuation, specific heat, nuclear resonant inelastic x-ray scattering spectroscopy, optical conductivity measurements in the terahertz time-domain or NMR relaxation were used to get a deeper understanding of the guest–host interactions and their influence on the thermal transport in the type-I $A_8\text{Ga}_{16}\text{Ge}_{30}$ clathrates ($A = \text{Eu}, \text{Sr},$

and Ba) and type-VIII $\text{Ba}_8\text{Ga}_{16}\text{Sn}_{30}$ clathrates.^{38–47} In particular, the guest free space, which depends on the ionic size of the guest atoms relative to the size of the cages, has been shown to be an important parameter in determining the lattice thermal conductivity values as shown in the $A_8\text{Ga}_{16}\text{Ge}_{30}$ compounds for which the thermal conductivity decreases on going from Ba to Eu .⁴⁸ This decrease is accompanied by drastic changes in the thermal transport, the crystalline-like behavior in the Ba compound switching into a glass-like dependence for Sr and Eu . In addition to these techniques, inelastic neutron scattering (INS) experiments on both single-crystal and polycrystalline samples represent another powerful tool to investigate the vibrational properties of clathrates on both momentum and energy scales and to probe possible anharmonicity of the crystal lattice upon temperature variations.^{35,49–54} So far, INS measurements were mainly carried out on Ge- and Si-based type-I clathrates, while little attention was paid to the Sn-based analogs.

Single crystal and powder x-ray diffraction have shown that, depending on the preparation conditions, the $A_8\text{Sn}_{44}\square_2$ compounds ($A = \text{K}, \text{Rb}, \text{Cs}$, and \square is a vacancy) exhibit a superstructure, i.e., a fully ordered vacancy sublattice.^{55–59} These experiments have further revealed an order–disorder transition in the Rb and Cs compounds, which sets in at 353 and 363 K, respectively.^{55,56} This transition strongly influences the temperature dependence of the thermopower while, surprisingly, leaving the thermal transport practically unperturbed. In addition, the temperature dependence of κ was found to be typical of crystalline insulators with a pronounced low-temperature crystalline peak. Recently, Christensen *et al.*⁶⁰ reported INS measurements on the Cs and Rb compounds at temperatures ranging between 274 and 373 K, i.e., below and above the order–disorder transition. These measurements confirmed the secondary role played by this transition on the thermal properties of these compounds. However, no results below 273 K and on the K analog have been reported so far. Extending these experiments to lower temperatures may offer further insights into the anharmonicity of type-I Sn-clathrates and unveil possible systematic trends in the lattice dynamics on going from Cs to K .

Here, we report a detailed investigation of the lattice dynamics of type-I clathrates $A_8\text{Sn}_{44}\square_2$ ($A = \text{K}, \text{Rb}$, and Cs) using a combination of low-temperature specific heat measurements (2–300 K) and temperature-dependent INS experiments (50–420 K) performed on polycrystalline samples. The experimental results are further compared to lattice-dynamics calculations carried out on hypothetical vacancy-free clathrates $A_8\text{Sn}_{46}$.

II. COMPUTATIONAL AND EXPERIMENTAL DETAILS

A. *Ab initio* lattice dynamics calculations

All the calculations have been carried out on vacancy-free structure models $A_8\text{Sn}_{46}$ ($A = \text{K}, \text{Rb}$, and Cs) considering the primitive cubic crystal structure in the space group $Pm\bar{3}n$. The DFT calculations were carried out with the Vienna *Ab Initio* Simulation Package (VASP). The exchange–correlation energy functional was formulated by the Perdew–Burke–Ernzerhof generalized gradient approximation (PBE-GGA). Projector augmented wave potentials were utilized with Sn_d ($s2p2 + 14el$), K_{sv} ($3s3p4s + 9el$), Rb_{sv} ($4s4p5s + 9el$), and Cs_{sv} ($5s5p6s + 9el$) electronic configurations. The ionic positions, cell shape, and volume were optimized on a single cell for a minimum energy on

a Monkhorst k -mesh of $8 \times 8 \times 8$ with a precision of $1\text{e-}4\text{ eV}$ for electronic minimization and an energy cut-off of 350 eV . The lattice parameters derived are 12.6229 , 12.6546 , and 12.6998 \AA for K_8Sn_{46} , $\text{Rb}_8\text{Sn}_{46}$, and $\text{Cs}_8\text{Sn}_{46}$, respectively. Hellmann–Feynman forces were computed on a $2 \times 2 \times 2$ Monkhorst k -mesh and a displacement of atoms in non-equivalent directions by 0.05 \AA . The derived force constants (dynamical matrix elements) for the guest atoms A are listed in Table I.

Dispersion curves $\hbar\omega(\vec{q})$ along high-symmetry directions in reciprocal space, total and partial vibrational density of states $Z(\omega)$ and specific heat $C_v(T)$ were calculated by the so-called direct method or supercell approach using the software PHONON.⁶¹ After optimization of the crystal structure, single-point energy calculations were performed by displacing one at a time each of the inequivalent atoms in both positive and negative Cartesian directions. These calculations enable obtaining the Hellmann–Feynman forces, which act on all atoms in the unit cell. The dynamical matrix for every point in the reciprocal space was then generated and diagonalized to derive the eigenmodes and eigenfrequencies. $Z(\omega)$ was obtained from a calculation on a mesh of 5×10^5 q points. The thermodynamic and elastic properties were computed from $Z(\omega)$ within the harmonic approximation.

In order to illustrate the degree of participation of the different atoms to the phonon eigenvectors, i.e., the vibrational amplitudes of a given eigenstate, their participation ratios (PR) have been calculated within the harmonic approximation as defined by the expression⁶²

$$p(\omega) = \frac{(\sum_{i=1}^N |u_i(\omega_{\vec{q}})|^2)^2}{N \sum_{i=1}^N |u_i(\omega_{\vec{q}})|^4},$$

where \vec{q} is the phonon wavevector, $u_i = e^i(\vec{q})/\sqrt{M_i}$ are the atomic amplitudes with the phonon polarization vectors $e^i(\vec{q})$ of an atom i of mass M_i . For eigenstates to which all atoms contribute with approximately equal amplitudes, as it is the case for long-wavelength acoustic phonons, PR approaches a value of 1. For eigenstates whose eigenvectors are dominated by a few or even a single species only, as we may expect for strongly localized eigenmodes and thus preferentially optic phonons, the PR approaches the value on the order of $1/N$. With the atomic participation ratio (APR), we may shed more light on the individual contributions of the different atoms to the lattice dynamics at a given energy. The APR has been calculated by the expression⁶²

$$p_i(\omega) = \frac{|u_i(\omega_{\vec{q}})|^2}{\sqrt{N \sum_{i=1}^N |u_i(\omega_{\vec{q}})|^4}},$$

with $p(\omega) = (\sum_{i=1}^N p_i(\omega))^2$. The APR has been determined for the cations in the two cages (denoted as A1 and A2 atoms with $A = \text{Cs}$,

TABLE I. Force constants derived for the guest atoms A for the clathrates A_8Sn_{46} . The values are expressed in $\text{amu THz}^2 (=0.1036 \times 10^{-3} \text{ eV \AA}^{-2})$.

| | K_8Sn_{46} | $\text{Rb}_8\text{Sn}_{46}$ | $\text{Cs}_8\text{Sn}_{46}$ |
|---------------------|----------------------------|-----------------------------|-----------------------------|
| $2a$ | 6402.81 | 8638.97 (ratio 1.35) | 12 965.11 (ratio 2.02) |
| Amu | 39.1 | 85.5 (ratio 2.19) | 132.9 (ratio 3.40) |
| $6d_{xx}$ | 1758.94 | 3901.16 (ratio 2.22) | 6793.86 (ratio 3.86) |
| $6d_{yy} = 6d_{zz}$ | 1026.21 | 1461.39 (ratio 1.42) | 3262.27 (ratio 3.18) |

Rb , and K) and for the ensemble of all Sn atoms. Both the PR and APR were calculated applying a powder average lattice dynamics (PALD)-like technique, which consisted of calculating an average response using a random distribution of 3000 \vec{q} vectors within the first Brillouin zone.

B. Synthesis, structural characterization, and thermodynamic measurements

Polycrystalline samples of $\text{A}_8\text{Sn}_{46}\square_2$ ($A = \text{K}$, Rb , and Cs) samples were synthesized from high-purity elements (Sn shots, Chempur, 99.999% and alkali metal pieces, Chempur, 99.9%) in a sealed tantalum crucible. The mixture was melted using an induction furnace in an argon-filled glovebox and further homogenized by annealing for two weeks at 573, 673, and 773 K for the K, Rb, and Cs clathrates, respectively, in the sealed tantalum crucible placed in argon-filled quartz ampoules.

Structural characterization of the products was performed by powder x-ray diffraction (PXRD) at room temperature using a Guinier diffraction technique (Huber G670 camera, $\text{Cu-K}\alpha_1$ radiation, $5^\circ \leq 2\theta \leq 100^\circ$). For all three samples, these measurements did not reveal any secondary phases.

The diffraction patterns of the Rb and Cs compounds show superstructure reflections indexed with a $2a \times 2a \times 2a$ [$2a = 24.212$ (2) and 24.101 (2) \AA at 300 K for the Cs and Rb compounds, respectively] unit cell of the parent clathrate-I type of structure [space group $Ia\bar{3}d$, Fig. 1(b)], which is consistent with prior results.^{55–59} The superstructure originates from the ordering of vacancies in the 24-atom tetrakaidecahedral cages similar to $\text{Ba}_8\text{Ge}_{43}\square_3$.^{63,64}

The situation is more complex in the $\text{K}_8\text{Sn}_{46}\square_2$ clathrate, which displays, in addition to the parent type structure $Pm\bar{3}n$, a rich variety of different vacancy-ordering variants depending on the synthesis conditions.⁵⁹ The sample investigated in this work was characterized by selected area electron diffraction in a transmission electron microscope (Fig. 2). The unit cell shows a tetragonal distortion with $2a = 24.063$ (2) \AA and $2c = 24.007$ (2) \AA and can be described with a structure model in the space group $I4_2d$. The tetragonal superstructure implies that the K2 atoms are located in polyhedra with different numbers of vacancies and thus, a different number of Sn atoms [see Fig. 1(c)].

Specific heat measurements were carried out in the 2–300 K temperature range on small polycrystalline pieces of each material ($\sim 20\text{ mg}$) by a standard relaxation method using a physical property measurement system (PPMS, Quantum Design).

C. Neutron-scattering time-of-flight experiments

Inelastic neutron scattering measurements were performed from 420 K down to 50 K using the cold-neutron time-of-flight spectrometer IN6@ILL at the European neutron source Institut Laue-Langevin in Grenoble, France. The anti-Stokes response (energy gain of neutrons) of the polycrystalline samples wrapped in a flat aluminum sample holder ($\sim 15\text{ g}$ for each sample) was recorded with an incident wavelength of $\lambda = 4.14\text{ \AA}$. The high total scattering power of the samples (Table II) compensated the lack of thermal population enabling us to follow the inelastic signal down to 50 K. All measurements below 300 K were carried out in

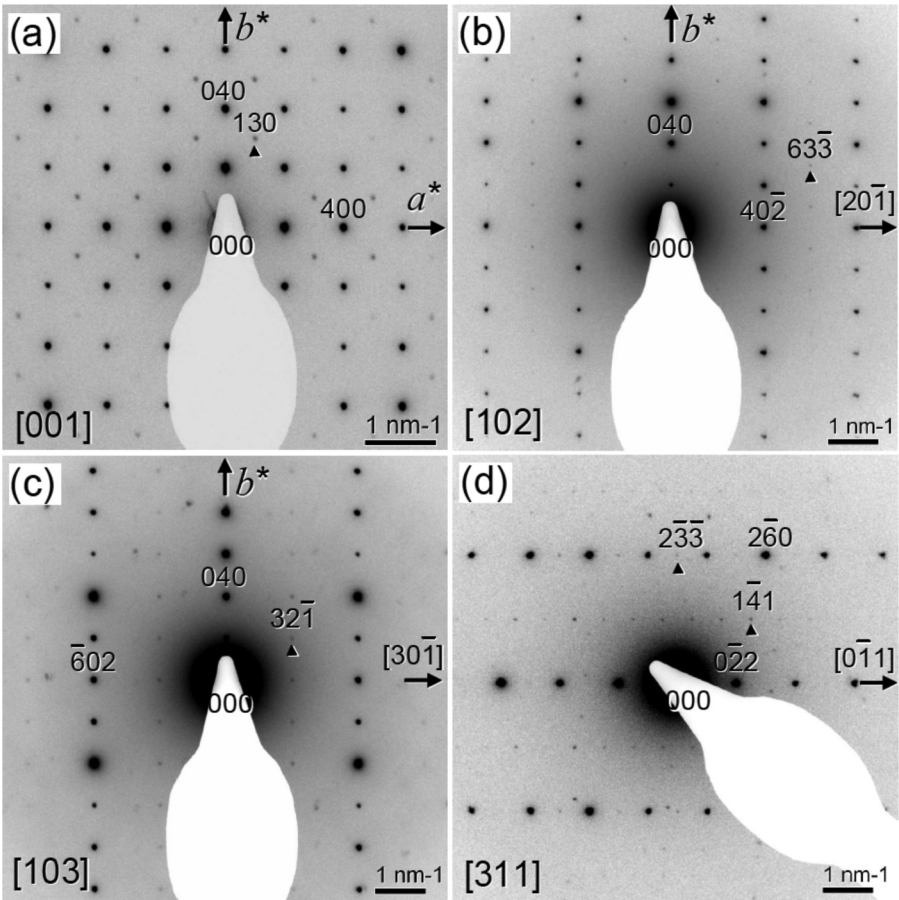


FIG. 2. Selected area electron diffraction (SAED) patterns of $\text{K}_8\text{Sn}_{44}\square_2$ with a tetragonal superstructure taken along the (a) [001], (b) [102], (c) [103], and (d) [311] directions. In the [001] direction [panel (a)], the superstructure reflections are particularly strong. In all panels, the superstructure reflections are indicated by black arrowheads.

cryostats in a helium atmosphere of about 10 mbar at 100 K. Above 300 K, a cryofurnace was utilized to collect data up to 420 K, i.e., above the temperature of the order–disorder transition of the $\text{Cs}_8\text{Sn}_{44}\square_2$ ($T = 363$ K) and $\text{Rb}_8\text{Sn}_{44}\square_2$ ($T = 353$ K) compounds.^{55,56} The resolution in the applied high-resolution inelastic-focusing mode ranges between 0.2 and 0.8 meV (full width at half maximum) in the energy range of 0.5 to 10 meV. Corrections were applied to the collected data for empty sample holder scattering and background and normalized to a vanadium standard to account for the efficiency of the multidetector banks. The experimental scattering functions $S(Q, \omega)$ were converted into the generalized vibrational

density of states $G(\omega)$ within the incoherent approximation.⁶⁵ All $G(\omega)$ spectra have been normalized to 162 phonon modes within the energy range of 0.5–25 meV. Thus, the exact stoichiometry and the variation in scattering power of the alloyed cations were not taken into account. Characteristic energies of peaks identified in $G(\omega)$ were evaluated by Gaussian least-square fits.

III. RESULTS AND DISCUSSION

A. Phonon dispersion curves and vibrational density of states $Z(\omega)$

The phonon dispersion curves calculated along high-symmetry directions are shown in Fig. 3(a) (left panels). The plots are restricted to the 0–10 meV energy range, that is, to the region of interest to shed light on the low-energy acoustic modes. Both the Cs and Rb compounds globally show similar dispersion relations above 4 meV. However, clear differences emerge below this energy [Fig. 3(b)]. A renormalization of the eigenfrequencies is observed in the Rb clathrate evidenced by a significant redshift of the optic modes near 2.5 meV at the zone boundaries and in the X–M–R direction. As a consequence, at the zone boundaries (X and M points), the energies of the acoustic modes are shifted toward lower energies on going

TABLE II. Coherent (σ_{coh}) and incoherent (σ_{inc}) neutron scattering cross sections (expressed in barns, i.e., 10^{-24} cm²), atomic mass M and total scattering power $\sigma_t/M = (\sigma_{coh} + \sigma_{inc})/M$ of the elements in the tin clathrates $\text{A}_8\text{Sn}_{44}\square_2$.

| Element | σ_{coh} | σ_{inc} | M | σ_t/M |
|---------|----------------|----------------|-------|--------------|
| K | 1.69 | 0.27 | 39.1 | 0.050 |
| Rb | 6.32 | 0.50 | 85.5 | 0.080 |
| Cs | 3.69 | 0.21 | 132.9 | 0.029 |
| Sn | 4.87 | 0.022 | 118.7 | 0.041 |

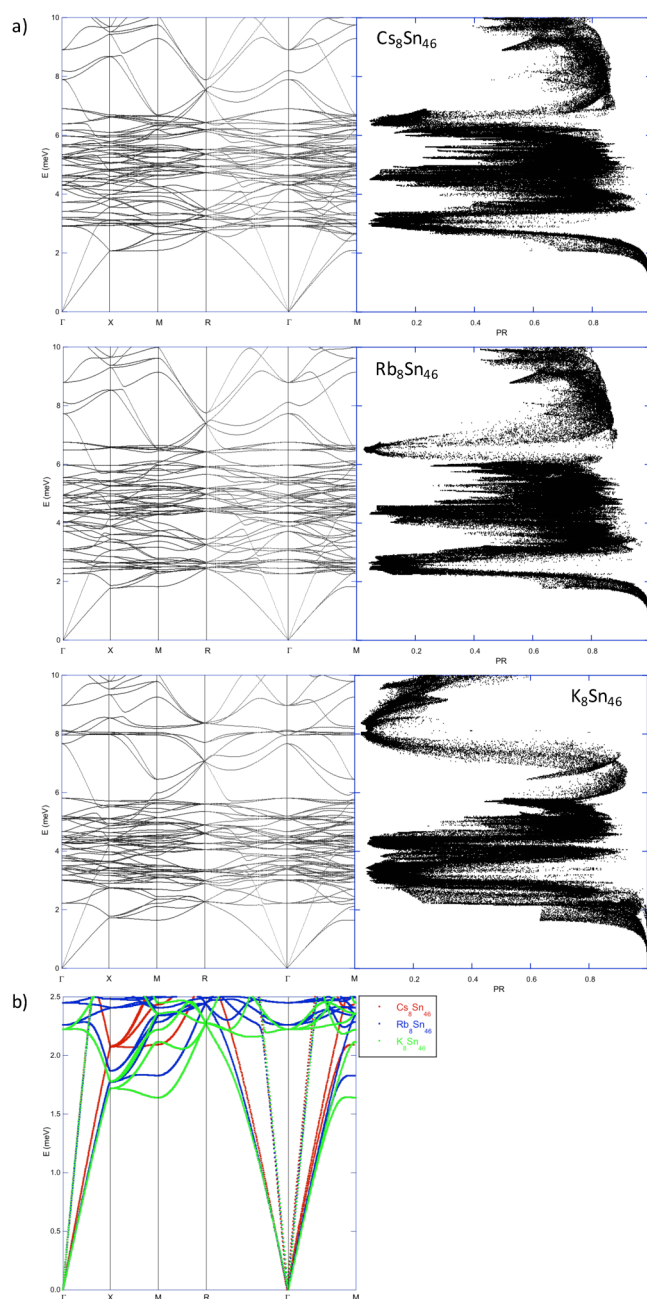


FIG. 3. (a) (Left panels) Phonon dispersion curves of the Cs (top), Rb (middle), and K (bottom) clathrates $A_8\text{Sn}_{46}$ calculated along high-symmetry directions. (Right panels) Participation ratio (PR) of the compounds calculated on a random mesh of 3000 \vec{q} points in the Brillouin zone. (b) Magnification of superimposed low-energy phonon dispersion curves of the clathrates $A_8\text{Sn}_{46}$.

from Cs to Rb. The effect of substituting K for Rb is more pronounced as the entire low-energy region (0–6 meV) is redshifted with respect to the Rb clathrate. This results in a further decrease in the acoustic phonon energies below 2 meV in the Γ -M and Γ -X

directions. Nevertheless, this shift is not accompanied by profound changes in the dispersion behavior of the acoustic phonons. In the K compound, the localization of eigenmodes sets in around 8 meV, while the eigenmodes of the Cs and Rb compounds display a more dispersive character. Hence, this localization results in an extended Q range in which, the phonon group velocity $\partial\omega(Q)/\partial Q$ is close to zero. The evolution of the acoustic dispersion curves on going from Cs to K [see Fig. 3(b)] highlights the dominant effect of guest–host interactions rather than the mass of the guest atoms. In none of the compounds, clear anti-crossing behavior occurs. The discrimination of the dispersion curves between back-folding or anticrossing rather depends on the eigenmode symmetry and direction in the Brillouin zone. This overall dependence of the dispersion curves on the nature of the guest atoms qualitatively resembles that observed in skutterudites $A\text{Fe}_4\text{Sb}_{12}$ ($A = \text{Ca}, \text{Ba}, \text{Sr}, \text{Yb}$, etc.) upon varying the entrapped cation A.^{66–69} The results obtained herein for the Cs compound are consistent with prior theoretical investigations.⁷⁰

These differences between the three compounds are further reflected by the participation ratio (PR) shown in Fig. 3(a) (right panels). Below 2 meV, all the compounds feature acoustic modes with a PR close to 1. Above this energy, non-propagative modes with low PR values set in and disrupt the acoustic phonon modes. This cut-off energy for the propagative modes increases with varying the nature of the cations following the sequence $\text{K} < \text{Rb} < \text{Cs}$. While the PR of both the Cs and Rb clathrates are qualitatively similar, clear differences are observed for the K clathrate between 6 and 10 meV, where the dispersive character of the modes changes from dispersive to localized with increasing energy. This sequence is reversed compared to that of the Rb and Cs clathrates for which a more dispersive character of the eigenmodes is observed upon increasing energy.

Figure 4 presents the calculated total phonon density of states $Z(\omega)$ along with the partial contributions for the three model compounds $A_8\text{Sn}_{46}$. $Z(\omega)$ was normalized to 162 modes to account for three degrees of freedom per atom in the unit cell. The partial contributions of the cations A1 (Wyckoff site 2a) and A2 (Wyckoff site 6d) and the framework atoms Sn1 (6c), Sn2 (16i), and Sn3 (24k) were normalized to 2, 6, 6, 16, and 24 atoms, respectively, according to the chemical stoichiometry. Regardless of the nature of the cations, the Sn framework dominates the high-energy region ($\hbar\omega > 10$ meV). The A-weighted mode intensities are mainly concentrated at energies below ~ 7 meV in the three compounds. In cage-like materials, the lowest energy modes can be usually directly related to the motion of the entrapped atoms with a pronounced spectral weight of the A2 atoms existing in the low-energy range for all compounds. This overall assignment of the vibrational modes is consistent with Raman experiments performed on the Cs and Rb compounds by Shimizu *et al.*⁷¹

These calculations further confirm that the A1 atoms do not contribute significantly to $Z(\omega)$ at low energies, their partial density of states being located above 5 meV. These states undergo a marked blueshift on going from Cs to K. Interestingly, the Sn-weighted modes extend to the low-energy region for all compounds, evidencing a well-defined guest–host coupling similar to that found for the Ge clathrates.²⁶ This effect is even more pronounced as the mass of the cation decreases.

In the Cs clathrate, the lowest Sn3 mode almost coincides with that of the Cs2 atoms, while for $A = \text{Rb}$, the Sn3-weighted mode

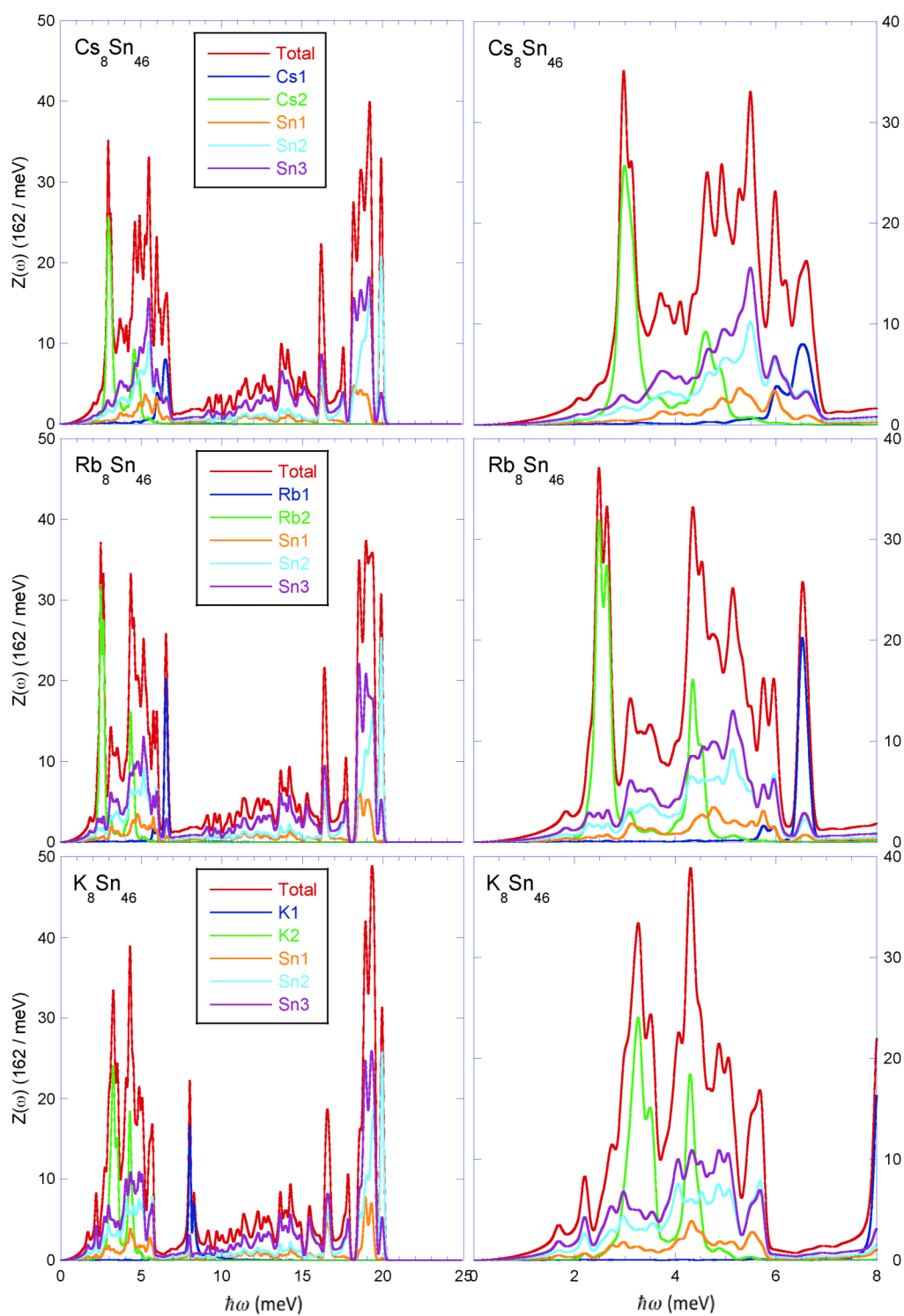


FIG. 4. (Left) Vibrational density of states $Z(\omega)$ of the vacancy-free clathrate compounds $A_8\text{Sn}_{46}$ as a function of the energy. The partial contributions from each atom are also shown. (Right) Magnification of the low-energy range where the modes of the A2 atoms are supposed to dominate.

appears at slightly lower energies. Eventually, in the K clathrate, the vibrational dynamics of the K2 atoms no longer gives rise to the lowest energy modes. Indeed, the Sn3-weighted modes dominate the lowest region of the spectrum. As we shall see below, these framework modes are clearly visible on the experimental GVDOS spectra of the Rb and K compounds, in agreement with the results obtained in the former by Christensen *et al.*⁶⁰

These findings can be better appreciated in Fig. 5, which shows the energy dependence of the atomic participation ratio (APR) of the cations in the small and large cages and of the Sn framework atoms. Below 2 meV, the APR is quasi-constant in energy in both the Cs and Rb clathrates with a nearly equivalent contribution from the A and Sn atoms as expected from acoustic modes near the Brillouin zone center. The optical phonon modes between 3 and 5 meV mostly consist of displacements of the A atoms in the large cages, while the A atoms in the small cages only give rise to optical phonons that dominate between 5 and 8 meV. These different contributions are qualitatively similar to the Ba₈Si₄₆ clathrate which does not feature vacancies in the Si framework.⁵² In contrast, the APR of the K clathrate significantly differs. Below 2 meV, the acoustic phonons involve an increased contribution of the Sn atoms, while the contribution of the K2 atoms in the large cages rapidly decreases with increasing energy up to about 2.1 meV. Above this energy, all the acoustic modes are localized and the optical phonons are mostly composed of motion of the K atoms in the large cages. Above 7 meV, the optical phonons consist in motions of the K atoms in the small cages, while the motion of the Sn framework atoms has only little contribution.

B. Generalized vibrational density of states $G(\omega)$ at 300 K

Figure 6(a) shows the generalized vibrational density-of-states $G(\omega)$ of the three Sn clathrates measured at 300 K. All the samples are characterized by a similar GVDOS spectrum with several peaks and shoulders that appear below the cut-off energy of ~ 25 meV. Regardless of the nature of the guest atoms, the $G(\omega)$ profile is dominated by two prominent peaks centered at $\hbar\omega \approx 6.5$ and 21 meV. Above ~ 12 meV, all the spectra merge indicating a similar lattice dynamics of the Sn framework. As shown in Table III, where the experimental positions of the modes observed in INS and Raman spectra for A = Cs and Rb are gathered, a very good agreement is achieved between both spectroscopic tools.⁷¹ However, we note that the lowest Raman mode measured in Cs₈Sn₄₄□₂ at 25 cm^{-1} (i.e., 3.1 meV) and assigned to the anisotropic thermal motion of the Cs atoms (Ref. 57) does not correspond to any obvious feature in our INS data.

Below ~ 12 meV, the low-energy peaks related to the dynamics of the guest atoms strongly depend on the nature of the alkali metal species. To stress the fine details in this energy window, a Debye plot $G(\omega)/\omega^2$ vs $\hbar\omega$ is shown in Fig. 6(b). At low energies, $G(\omega)/\omega^2$ is almost constant as expected from a Debye-like contribution for which $G(\omega) \propto \omega^2$. The Cs compound is characterized by a double-peak structure at $\hbar\omega \approx 4.1$ and 4.7 meV and a peak centered at 6.7 meV. Replacing Cs by Rb results in a rise in the intensity of the peaks at 4.7 and 9 meV. The second peak observed at

7 meV in the Cs compound is slightly shifted toward lower energy in the Rb clathrate ($\hbar\omega \approx 6.4$ meV). The lattice dynamics of the K compound is characterized by a single peak at 4.5 meV together with an additional peak at lower energy ($\hbar\omega \approx 3.3$ meV) that can be assigned to Sn-weighted modes according to our calculations. The peak near 9 meV, visible in the Cs and Rb compounds, seems to split into two peaks shifted to 9.5 and 10.5 meV in the K clathrate. In both Cs₈Sn₄₄□₂ and Rb₈Sn₄₄□₂, this peak has been tentatively attributed to either a vacancy-induced localized vibration or a vacancy-induced intensity enhancement of a weak Raman mode.⁷¹ In light of our calculations, this peak may be rather ascribed to the dynamics of the Cs1 and Rb1 atoms. Above 17 meV, no significant differences between the three spectra are observed due to the similar contributions of the Sn framework atoms to the GVDOS.

Our *ab initio* lattice dynamics calculations reproduce the general features of the three measured GVDOS [Figs. 6(c) and (d)], that is, the main block of low-energy states below 9 meV and the last peak near 19 meV, both separated by a region where the PDOS is significantly reduced for all compounds. In addition, the blueshift of the mode that appears at 9 meV in the Cs and Rb compounds to 11 meV in the K compound is also observed in the computed spectra as a shift from about 6 to 8 meV. Another distinct characteristic well captured in these calculations is the first modes that show up near 3.2 meV in the K clathrate (2 meV in the computed spectra), that is, at significantly lower energy than in the Cs and Rb compounds. However, the agreement between theory and experiment is not entirely satisfying. The overall calculated spectra are shifted toward lower energies in comparison to the experimental data. In addition, the relative intensities between the two main blocks of modes (0–9 meV and 17–20 meV) are not well reproduced in the calculations. We attribute these differences to a pronounced localization effect in the dynamics of the DFT generated compounds, whose origin might be the ordered, vacancy free structures used therein. Nevertheless, these calculations provide a useful piece of information regarding the origin of the low-energy modes and the general trend in the lattice dynamics on going from Cs to K. Future theoretical studies taking into account the ordered vacancy sublattice and the tetragonal distortion in the K compound may provide further insights into their role on the lattice dynamics of these type-I clathrates.

C. Temperature dependence of $G(\omega)$

The response of the inelastic signal upon cooling from 420 K down to 50 K is depicted in Figs. 7(a), 7(c), and 7(e) in the whole energy range. Note that the increase in the intensity upon cooling is a direct consequence of the concomitant decrease in the Debye–Waller factors of the atoms. As mentioned previously, an order–disorder transition sets in at 353 and 363 K in Rb₈Sn₄₄□₂ and Cs₈Sn₄₄□₂, respectively.^{55,56} Raman spectroscopy performed on the former between 293 and 369 K revealed slight changes in the mode at 70 cm^{-1} (i.e., 8.7 meV) and in the Sn-weighted modes around $165\text{--}170\text{ cm}^{-1}$ (i.e., 20.4–21.1 meV).⁷¹ Our INS data do not corroborate these findings since no obvious changes are observed. In any case, the similar GVDOS measured below and above the transition temperature confirm that

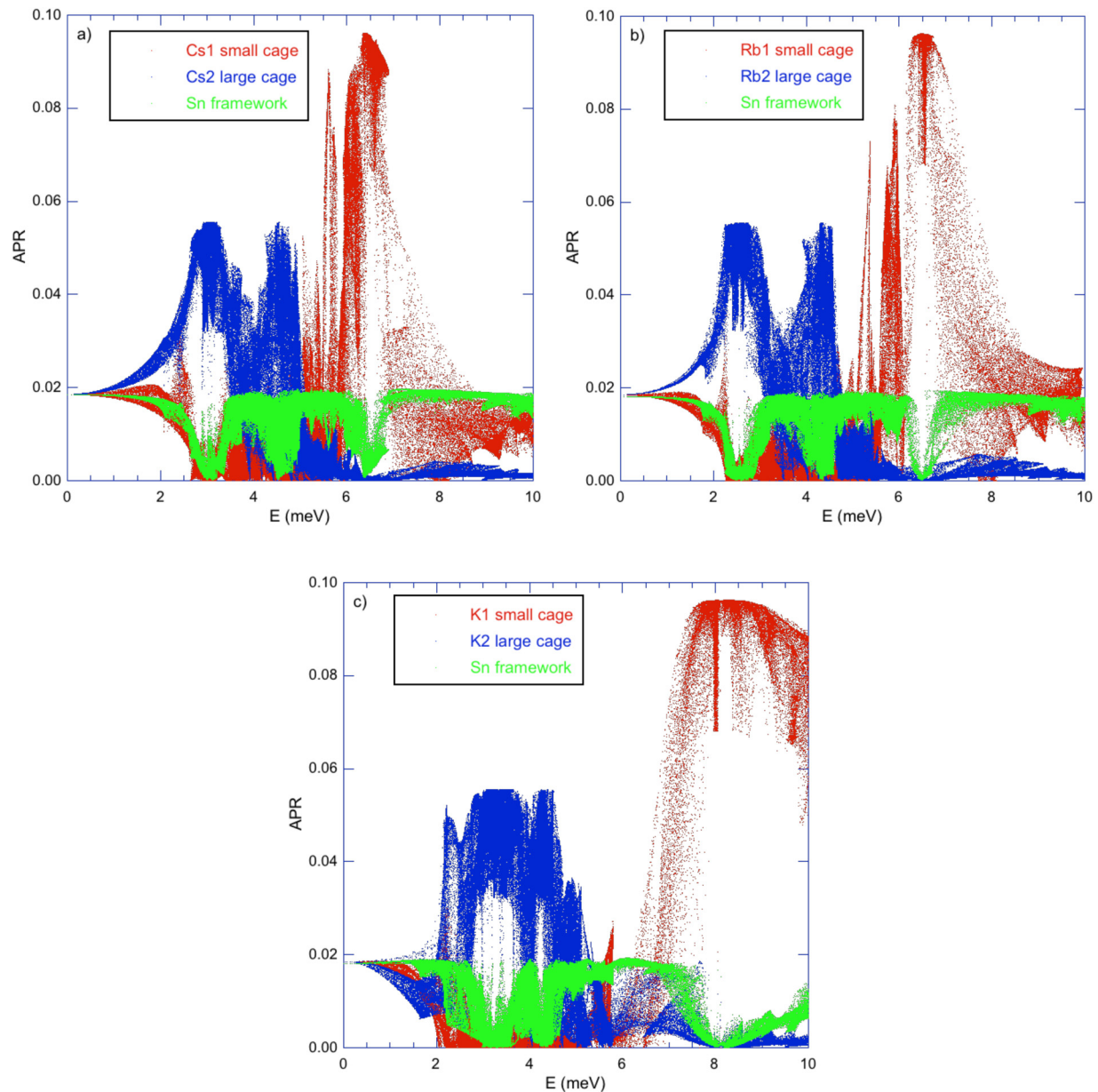


FIG. 5. Atomic participation ratio (APR) obtained by a powder average lattice dynamics approach for the (a) Cs, (b) Rb, and (c) K clathrates $A_8\text{Sn}_{46}$. In each panel, the APR has been calculated for the Cs, Rb, and K atoms in the large and small cages and for all the Sn framework atoms.

this transition plays only a minor role in determining the thermal properties of these compounds.

For all compounds, the overall phonon spectrum shifts upon cooling toward higher energy due to the thermal contraction of the unit cell. This trend is clearly visible, for instance, on the peak at 5 meV in the K compound and at 6.5 meV in the Rb and Cs compounds [Figs. 7(b), 7(d), and 7(f)]. In addition to a

sharpening of the peaks upon cooling, one of the main features is related to the appearance of an additional well-defined peak at 9 meV in the K compound (Fig. 8). This peak, absent in the data measured at 300 and 420 K, is clearly visible at 100 K and still discernible at 50 K. Its position corresponds to the peaks observed around the same energy in the Cs and Rb compounds, which exhibit a significant spectral weight of the Cs1 and Rb1

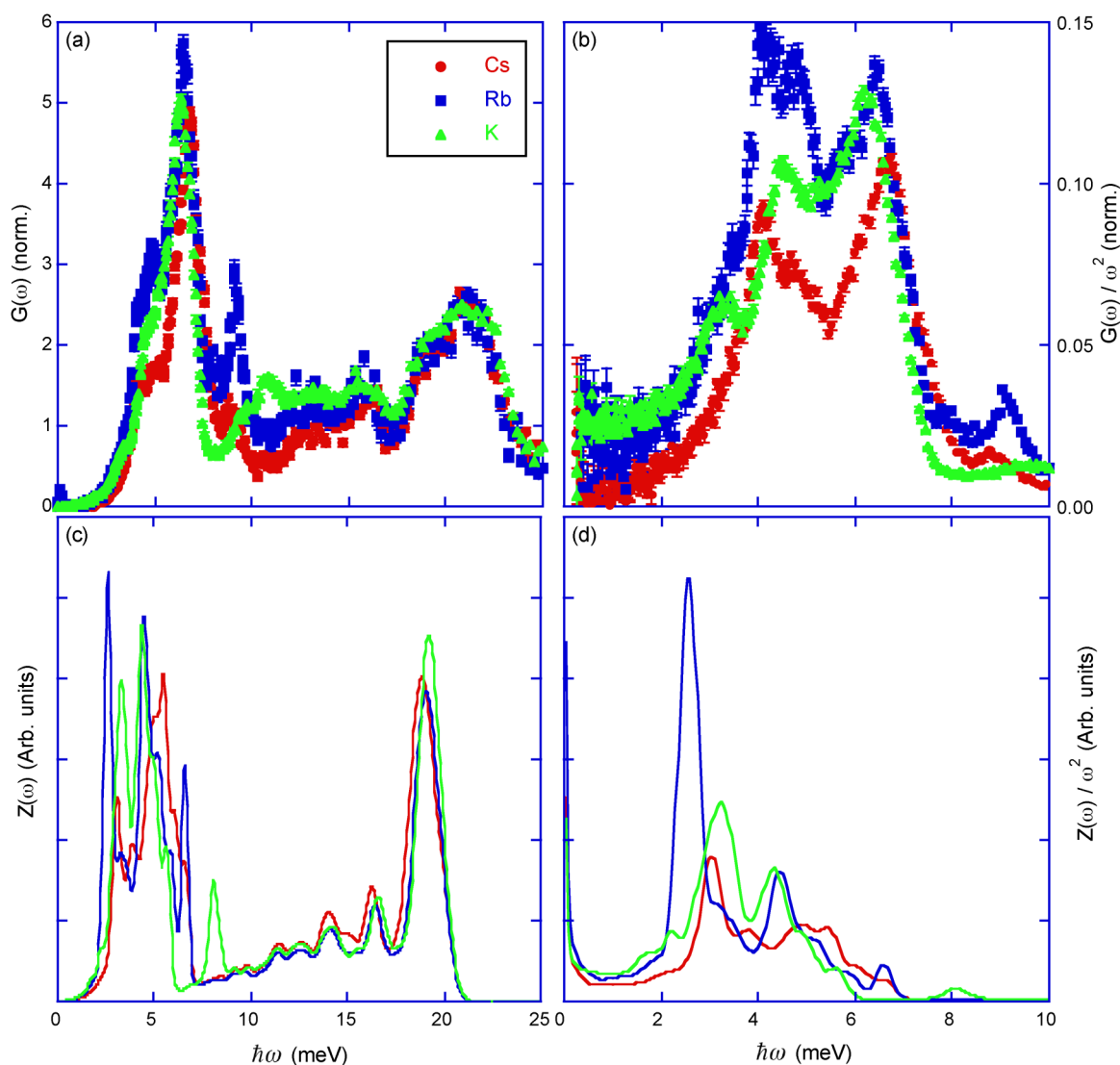


FIG. 6. Comparison between the generalized density of states $G(\omega)$ of the Cs₈Sn₄₄□₂, Rb₈Sn₄₄□₂, and K₈Sn₄₄□₂ compounds measured at 300 K at IN6@ILL [panels (a) and (b)] and the calculated vibrational density of states $Z(\omega)$ [panels (c) and (d)]. The experimental data were normalized according to the intensity of the high-energy peaks ($\hbar\omega \approx 20$ meV) and the $Z(\omega)$ data were convolved with a Gaussian function to approximate the energy-dependent resolution of the IN6 spectrometer. The panels (b) and (d) show the low-energy range of $G(\omega)/\omega^2$ to highlight the structure of the low-energy region of the PDOS spectra.

atoms. Hence, this peak may be tentatively ascribed to the dynamics of the K1 atoms.

Another common behavior shared by the three compounds is tied to the softening of the low-energy peaks as the temperature decreases. Noteworthy, this effect is not restricted to the A2 cation-weighted modes but is also observed for the Sn-weighted mode in the K compound. The softening does not depend on the nature of the A atoms even though the amount by which they are shifted slightly varies. This can be more easily visualized in Fig. 9 where the positions of the lowest-energy peaks are shown as a function of

temperature. The softening in Cs₈Sn₄₄□₂ and K₈Sn₄₄□₂ is of comparable magnitude, while it seems to be slightly higher in Rb₈Sn₄₄□₂, particularly above 300 K.

To shed light on possible anharmonic behavior of the guest atoms, we tried to describe the temperature dependence of the low-energy features following the model proposed by Dahm and Ueda.⁷² This model was initially developed with the aim of studying the influence of a localized anharmonic phonon on the electrical resistivity and NMR relaxation rate in pyrochlores. Using this model to predict the softening of a phonon mode upon cooling

TABLE III. Comparison of the phonon modes observed in the INS data of $\text{Cs}_8\text{Sn}_{44}\square_2$ and $\text{Rb}_8\text{Sn}_{44}\square_2$ with those identified in the Raman spectra reported in Ref. 71. The modes seen in both compounds at 15.9 meV correspond to a weak maximum in the Raman spectra that might explain why these modes were not assigned to an active mode.

| $\text{Cs}_8\text{Sn}_{44}\square_2$ | | | $\text{Rb}_8\text{Sn}_{44}\square_2$ | | |
|--------------------------------------|-------------------------------|----------------------------------|--------------------------------------|-------------------------------|----------------------------------|
| INS (meV) | Raman (cm^{-1}) | Observed (cm^{-1}) | INS (meV) | Raman (cm^{-1}) | Observed (cm^{-1}) |
| 4.19 | 34 | 32 | 4.26 | 34.4 | 34 |
| 6.64 | 54 | 53 | 4.82 | 39.0 | 40 |
| 8.92 | 72 | 73 | 6.47 | 52.2 | 51 |
| 13.0 | 105 | 100 | 9.29 | 75.0 | 73 |
| 15.9 | 128 | / | 13.0 | 105 | 102 |
| 21.2 | 171 | 167 | 15.9 | 128 | ... |
| | | | 19.3 | 156 | 155 |
| | | | 21.8 | 175 | 165 |

may thus provide valuable information on its anharmonicity. The temperature dependence of a phonon of frequency ω_0 is derived from the nonlinear equation⁷²

$$\left(\frac{\omega_0}{\omega_{00}}\right)^2 = 1 + \beta \frac{\omega_{00}}{\omega_0} \left(\frac{1}{\frac{\hbar\omega_0}{e^{k_B T}} - 1} + \frac{1}{2} - \frac{1}{2} \frac{\omega_0}{\omega_{00}} \right), \quad (1)$$

where ω_{00} is the phonon frequency in the zero temperature limit $\omega_{00} = \omega_0(T = 0)$ and β is a dimensionless parameter that measures the strength of the anharmonicity. Figure 9 shows a comparison between the theoretical and experimental temperature dependences of the low-energy phonon mode in the $\text{A}_8\text{Sn}_{44}\square_2$ series. For all compounds, the experimental $\omega(T)$ curve is well reproduced using a β parameter of ~ 0.025 indicative of weak anharmonicity. This value is one order of magnitude lower than that required to describe the strong softening of the lowest energy peak in KOs_2O_6 ($\beta \approx 0.7$), $\text{Cu}_{12}\text{Sb}_2\text{Te}_2\text{S}_{13}$ ($\beta \approx 0.5$), and two orders of magnitude lower compared to the record value measured recently in $\text{GaV}_2\text{Al}_{20}$ ($\beta \approx 20$).^{3,73–75} The fact that the temperature dependence of these low-energy modes above 50 K does not significantly deviates from a quasi-harmonic behavior suggests that the A atoms experience a practically temperature-independent potential inside the tetrakaidecahedra. Although similar conclusions were drawn in various Ge- and Si-based clathrates with Ba as the guest atom, additional measurements down to 4 K would be interesting to ascertain this point. In addition to the above-mentioned pyrochlores, a systematic study of the lattice dynamics with varying the nature of the encaged cation from K to Cs has been recently realized in the Al-doped defect pyrochlore tungstates $\text{AA}_{0.33}\text{W}_{1.67}\text{O}_6$.⁷⁶ In both families, a distinct dynamics of K was evidenced not only due to the lighter mass and smaller size of K with respect to Rb and Cs but also owing to the anharmonic potential felt by K in the oversized cages. However, this pronounced anharmonicity in the K compounds is not shared by these type-I clathrates, which is possibly due to the different vacancy ordering observed in $\text{K}_8\text{Sn}_{44}\square_2$.

D. Specific heat

The fact that the free-electron relation $C_p/T = \gamma + \beta T^2$ only describes the data adequately in a narrow temperature window in type-I clathrates is well documented in both Ge- and Si-based clathrates. Sn-based compounds are no exception to this behavior. The electronic and phonon contributions γT and βT^3 , respectively, were determined from the best fit to the data following the above-mentioned relation. For all samples, this analysis results in γ values indistinguishable from zero to within experimental uncertainty reflecting their semiconducting nature. Within the Debye theory, the β values are related to the Debye temperature θ_D via $\theta_D = (12\pi^4 n R / 5\beta)^{1/3}$, where n and R are the number of atoms per formula unit and the ideal gas constant, respectively. The low θ_D values (~ 160 K) are in good agreement with those determined for the Cs and Rb compounds from the temperature dependence of the isotropic thermal displacement parameters U_{iso} by Kaltzoglou *et al.*⁵⁶

A comparison between the experimental specific heat C_p and the theoretical specific heat C_v computed from the PDOS $Z(\omega)$ (see Fig. 4) is shown in Fig. 10. The experimental data are shown as C_p/T^3 as a function of T between 1.9 and 100 K to stress the temperature range, where the dynamics of the A2 cation is expected to dominate. In this temperature range, we assume that anharmonic effects are negligible so that $C_p(T) \approx C_v(T)$ which allows for a direct comparison between both sets of data. The overall match between the measured and calculated data is qualitatively good. The calculations reproduce well the excess specific heat near 10 K originating from the low-energy phonon modes as well as the sequence of the maxima (Cs < K < Rb). Within a simple harmonic oscillator model assuming a spring constant, the lower mass of K compared to Cs and Rb should give rise to higher vibration frequency. Therefore, the sequence Cs < Rb < K may be expected. The observed difference may reflect the Sn-weighted modes that contribute at low energies in the K clathrate. As evidenced in the type-I clathrates $\text{A}_8\text{Ga}_{16}\text{Ge}_{30}$ (A = Sr, Ba, and Eu),³¹ the small ionic radius of the guest atom relative to the radius of the cage plays also an important role for decreasing the energy of the thermal vibrations of the guest atoms. Thus, the smaller ionic radius of K compared to Rb and Cs may contribute to explain the distinct behaviour of the K clathrate with respect to the Cs and Rb clathrates. Nevertheless, the calculations overestimate the low-temperature $C_p(T)$ for all compounds due to the positions of the low-energy modes that are calculated at lower energies than experimentally observed in $G(\omega)$.

In type-I clathrates, a self-consistent description of the low-temperature C_p data is usually obtained by including Einstein terms that model the thermal motion of the guest atoms. This model assumes that the low-temperature peak in C_p solely originates from the guest atoms and hence, does not take into account the non-negligible contribution of the framework atoms at low energies as shown by the computed APR in Fig. 5. Prior crystallographic investigations have further shown that only the cations entrapped in the tetrakaidecahedra (A2 atoms) may be considered to behave as Einstein oscillators. In this context, the low-temperature $C_p(T)$ data are then modeled by a combination of Debye and Einstein terms

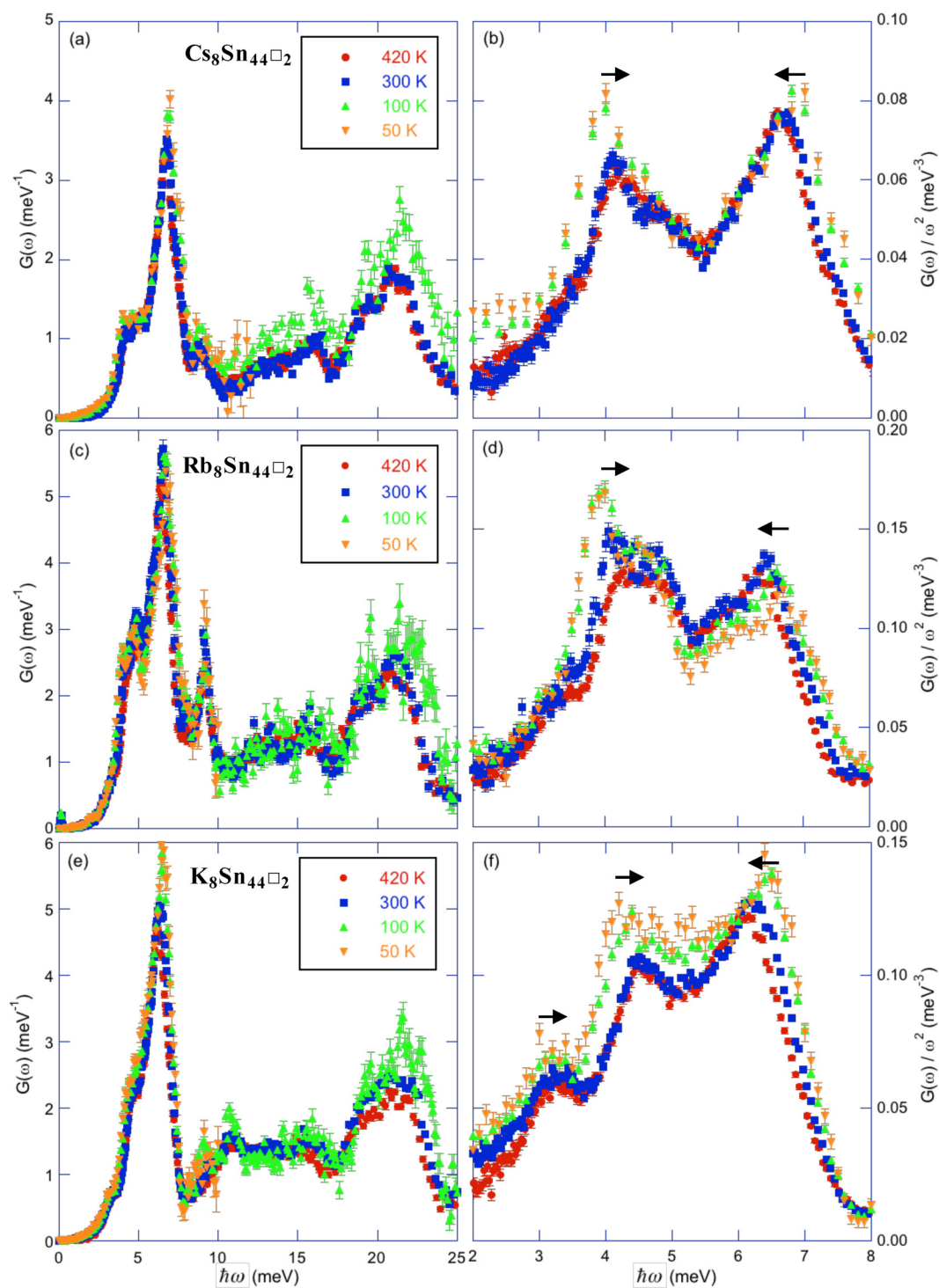


FIG. 7. Temperature dependence of the generalized density of states $G(\omega)$ of the $\text{Cs}_8\text{Sn}_{44}\square_2$ [(a) and (b)], $\text{Rb}_8\text{Sn}_{44}\square_2$ [(c) and (d)] and $\text{K}_8\text{Sn}_{44}\square_2$ [(e) and (f)] compounds measured at IN6@ILL. The panels on the right show data plotted as $G(\omega)/\omega^2$ vs $\hbar\omega$ to stress the softening upon cooling of the low-energy peaks. The black arrows in panels (b), (d), and (f) show the direction of the shift of the low-energy peaks upon heating.

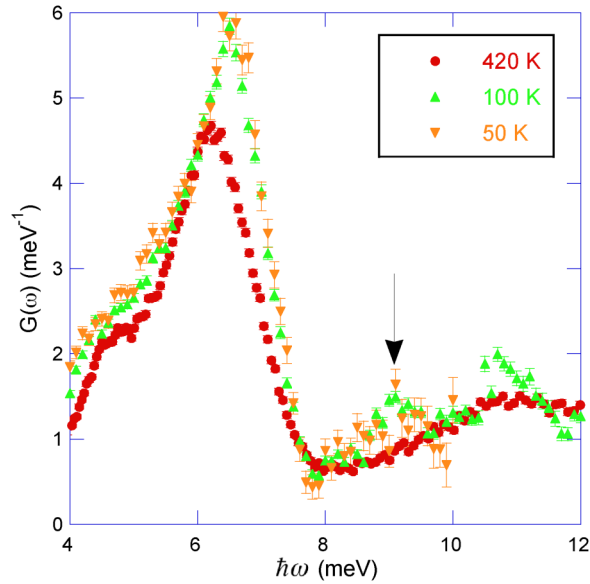


FIG. 8. Magnification of $G(\omega)$ of the $\text{K}_8\text{Sn}_{44}\square_2$ compound in the energy range where an additional peak appears at $\hbar\omega \approx 9$ meV (marked by the black arrow).

through the relation^{14,28,63,77–82}

$$C_p = C_D + C_{Ei}$$

$$= 9N_D R \left(\frac{T}{\theta_D} \right)^3 \int_0^{\theta_D/T} \frac{x^4 e^x}{(e^x - 1)^2} dx + \sum_i p_i N_{Ei} R \left(\frac{\theta_{Ei}}{T} \right)^2 \frac{e^{\theta_{Ei}/T}}{(e^{\theta_{Ei}/T} - 1)^2}, \quad (2)$$

where C_D is the lattice contribution described within the Debye model, C_{Ei} is the Einstein contribution of the i th vibrational mode of the guest atoms, $x = \hbar\omega/k_B T$ with \hbar being the reduced Planck constant and k_B the Boltzmann constant, N_D is the number of Debye oscillators per formula unit and p_i , N_{Ei} , and θ_{Ei} are the degrees of freedom, the number of Einstein oscillators, and the Einstein temperature related to the i th vibrational mode, respectively. If we further take into account the anisotropic thermal displacement of the guest atoms, two Einstein terms associated to the two-dimensional in-plane (θ_{E1}^{\parallel}) and one-dimensional out-of-plane (θ_{E2}^{\perp}) vibrations should be considered. As a first step, the numbers of Debye and Einstein oscillators together with the degrees of freedom were constrained to be equal to $N_D = 46$ (44 Sn plus 2 Al atoms), $p_{E1}^{\parallel} N_{E1}^{\parallel} = 2 \times 6$ and $p_{E2}^{\perp} N_{E2}^{\perp} = 1 \times 6$. In a second step, we considered several models allowing for either the Einstein temperatures, the spectral weights or both to vary. The different models considered for each compound as well as the values of the fitting parameters determined from the best fits to the data are listed in Table IV.

A first interesting outcome of this analysis is the equal values found for the Cs compound, which suggests a nearly-isotropic behaviour of the Cs thermal vibrations. Of note, using only one Einstein term in Eq. (2) yields a fit of similar quality with the nearly same Einstein temperature. This result agrees well with our INS data that did not evidence a clear separation of the peaks around 4 meV in the Cs sample in contrast to the Rb compound for which a shoulder at lower energies is clearly discernible. The values derived for $\text{Rb}_8\text{Sn}_{44}\square_2$ are in excellent agreement with the low-energy phonon modes observed both in the Raman and INS spectra (see Table III) but slightly lower than the Einstein temperatures inferred from the temperature dependence of the $U_{ij}(T)$ parameters.⁵⁶ As outlined in skutterudite compounds, the mismatch between the Einstein temperatures derived from thermal displacement parameters and specific heat data is likely the result of the contribution of the cations to eigenmodes at higher energies.

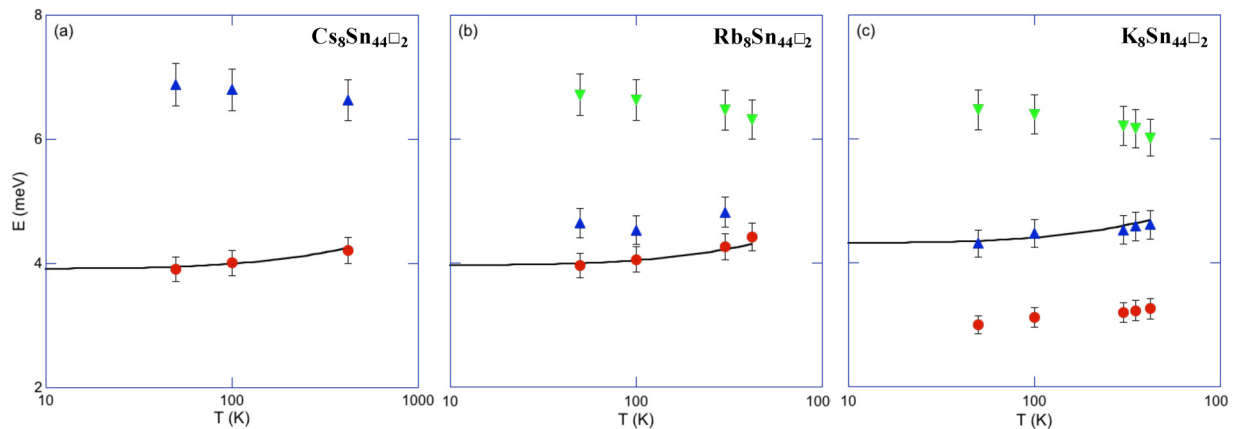


FIG. 9. Temperature dependence of the position of the low-energy peaks of the $\text{Cs}_8\text{Sn}_{44}\square_2$ (a), $\text{Rb}_8\text{Sn}_{44}\square_2$ (b), and $\text{K}_8\text{Sn}_{44}\square_2$ (c) clathrates. For the Cs compound, only the variations in temperature of the two main peaks near 4 and 7 meV are reported, while the peaks near 4, 4.8, and 6.5 meV are shown for the Rb compound. For the K compound, the peaks near 3.2, 4.5, and 6.2 meV are presented [see panels (b), (d), and (f) of Fig. 7]. For all panels, the solid black line stands for the theoretical temperature dependence according to Eq. (1) with $\beta = 0.025$.

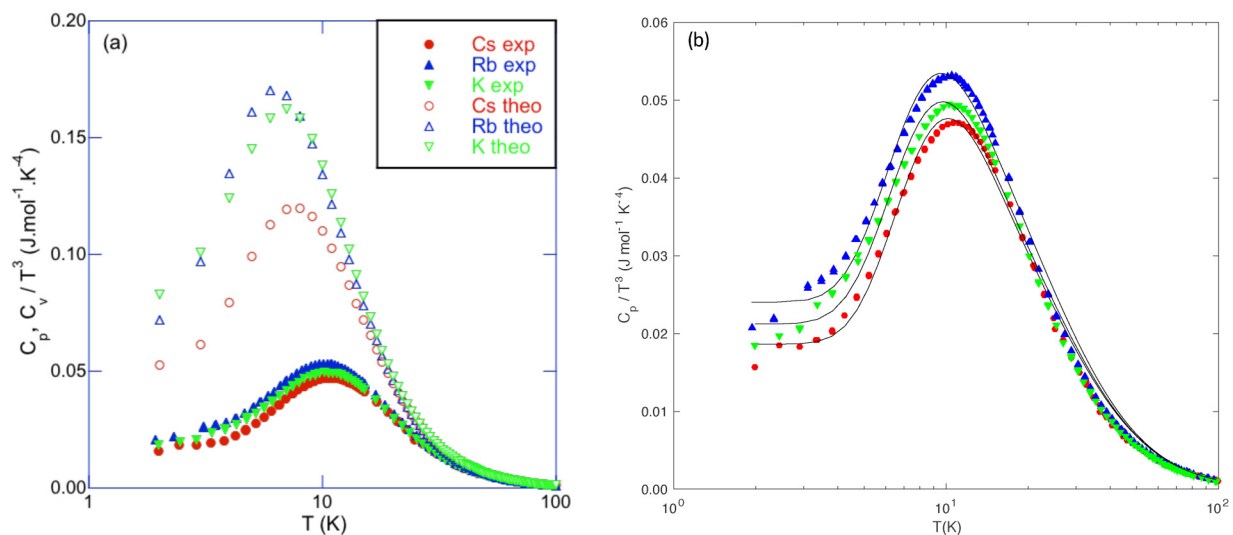


FIG. 10. (a) Comparison between the measured $C_p(T)$ (filled symbols) and theoretical $C_v(T)$ (open symbols) data plotted as $(C_p \text{ or } C_v)/T^3$ vs T for the $A_8\text{Sn}_{44}\square_2$ clathrates. (b) $C_p(T)/T^3$ plotted as a function of T on a logarithmic scale to highlight the excess specific heat superimposed on a Debye background. The black solid line stands for the best fits to the data according to Eq. (2) with fixed numbers of Einstein oscillators and two Einstein temperatures used as free parameters (model III in Table IV).

For both compounds, keeping constant the Einstein temperatures to the values corresponding to the lowest energy modes observed in the INS spectra (model V in Table IV) results in numbers of Einstein oscillators $p_{E1}^{\parallel}N_{E1}^{\parallel}$ and $p_{E2}^{\perp}N_{E2}^{\perp}$ that are in fair agreement with the aforementioned values.

For $\text{K}_8\text{Sn}_{44}\square_2$, this model captures equally well the temperature dependence of the excess C_p . The values inferred (see Table IV) are

comparable to those obtained for the Cs and Rb compounds and in line with the peak observed near 4.5 meV in $G(\omega)$. However, none of the models considered is able to reproduce the lowest-energy peak in $G(\omega)$ (near 3.2 meV) that would correspond to an Einstein temperature of 37 K. Alternatively, fixing the Einstein temperatures between 37 and 51 K yields a very low spectral weight for the lowest energy mode which significantly differs from those determined for the Cs

TABLE IV. Values of the fitting parameters inferred from fits to the $C_p(T)$ data shown in Fig. 10. For each model considered, the parameters that were allowed to vary during the least-squares refinements are indicated in parenthesis. For all models, the number of Debye oscillators was kept constant and equal to the sum of 44 Sn atoms and 2 A atoms; only the A atoms in the tetrakaidecahedra were considered as Einstein oscillators.

| $\text{Cs}_8\text{Sn}_{44}\square_2$ | θ_D (K) | N_{E1} | θ_{E1}^{\parallel} (K) | N_{E2} | θ_{E2}^{\perp} (K) |
|---|----------------|----------|-------------------------------|----------|---------------------------|
| I (θ_D, θ_{E1}) | 166 | 18 | 48.8 | ... | ... |
| II ($\theta_D, N_{E1}, \theta_{E1}$) | 169 | 20.5 | 50.0 | ... | ... |
| III ($\theta_D, \theta_{E1}, \theta_{E2}$) | 166 | 12 | 48.7 | 6 | 48.7 |
| IV ($\theta_D, N_{E1}, \theta_{E1}, N_{E2}, \theta_{E2}$) | 169 | 10.2 | 50.1 | 10.2 | 50.1 |
| V (θ_D, N_{E1}, N_{E2}) | 169 | 9.5 | 48.6 | ... | ... |
| $\text{Rb}_8\text{Sn}_{44}\square_2$ | θ_D (K) | N_{E1} | θ_{E1} (K) | N_{E2} | θ_{E2} (K) |
| I (θ_D, θ_{E1}) | 155 | 18 | 47.5 | ... | ... |
| II ($\theta_D, N_{E1}, \theta_{E1}$) | 154 | 17.4 | 47.2 | ... | ... |
| III ($\theta_D, \theta_{E1}, \theta_{E2}$) | 155 | 12 | 45.4 | 6 | 53.2 |
| IV ($\theta_D, N_{E1}, \theta_{E1}, N_{E2}, \theta_{E2}$) | 155 | 10.2 | 44.6 | 8.0 | 52.8 |
| V (θ_D, N_{E1}, N_{E2}) | 153 | 14.8 | 49.4 | 6.2 | 55.9 |
| $\text{K}_8\text{Sn}_{44}\square_2$ | θ_D (K) | N_{E1} | θ_{E1} (K) | N_{E2} | θ_{E2} (K) |
| I (θ_D, θ_{E1}) | 162 | 18 | 48.0 | ... | ... |
| II ($\theta_D, N_{E1}, \theta_{E1}$) | 161 | 17.6 | 47.9 | ... | ... |
| III ($\theta_D, \theta_{E1}, \theta_{E2}$) | 161 | 12 | 46.0 | 6 | 53.4 |
| IV ($\theta_D, N_{E1}, \theta_{E1}, N_{E2}, \theta_{E2}$) | 162 | 11.8 | 45.6 | 6.4 | 54.7 |
| V (θ_D, N_{E1}, N_{E2}) | 163 | 2.1 | 37.1 | 17.5 | 51.0 |

and Rb clathrates. The fact that none of these models captures well the lowest-energy peak in $G(\omega)$ clearly shows that this peak cannot be modeled as an Einstein oscillator. The inadequacy of this analysis further confirms that this peak arises from the dynamics of the framework atoms rather than solely from that of the K2 atoms.

IV. CONCLUSIONS

The joint theoretical and experimental investigation on the vibrational properties of the type-I clathrates $A_8\text{Sn}_{44}\square_2$ ($A = \text{Cs}$, Rb , and K) revealed characteristic trends of the lattice dynamics upon varying the mass and the size of the cations. The *ab initio* calculations are in fair agreement with the experimental observations, the former reproducing several characteristic features on going from Cs to K. The temperature response of the inelastic signal followed between 50 and 420 K evidenced only a weak anharmonic behavior of the thermal vibrations of the A2 atoms that does not depend on the nature of the alkali element. This conventional quasi-harmonic character observed above 50 K is consistent with specific heat analyses, which show that a simple phenomenological model that includes a restricted set of temperature-independent parameters is sufficient to describe the low-temperature variations in C_p . The order-disorder transition undergone by the Cs and Rb compounds does not lead to significant changes in the GVDOS spectra to within experimental uncertainty. Unlike other families of cage-like materials in which stronger anharmonicity is observed in the K-containing compounds, the behavior of the K clathrate can be well approximated by a quasi-harmonic model above 50 K. This difference may be attributed to a stronger coupling of the cations with the Sn framework atoms, which results in Sn-weighted modes that dominate the low-energy GVDOS of this compound. Finally, it would be instructive to perform INS experiments on Ge- and Si-based analogs with Cs, Rb, and K as guest atoms to determine whether a similar situation emerges.

ACKNOWLEDGMENTS

C.C. acknowledges financial support of the CNRS-MPG program. The ILL College 7 is acknowledged for the support of this work and the grant of accessing the IN6 instrument of the European neutron source Institut Laue-Langevin. M.M.K. acknowledges the access to ILL's "Scientific Computing" facility.

REFERENCES

- ¹K. Suekuni, K. Tsuruta, T. Ariga, and M. Koyano, *Appl. Phys. Express* **5**, 051201 (2012).
- ²X. Lu, D. T. Morelli, Y. Xia, F. Zhou, V. Ozolins, H. Chi, X. Zhou, and C. Uher, *Adv. Energy Mater.* **3**, 342 (2013).
- ³Y. Bouyrie, C. Candolfi, S. Pailhès, M. M. Koza, B. Malaman, A. Dauscher, J. Tobola, O. Boisson, L. Saviot, and B. Lenoir, *Phys. Chem. Chem. Phys.* **17**, 19751 (2015).
- ⁴P. Qiu, T. Zhang, Y. Qiu, X. Shi, and L. Chen, *Energy Environ. Sci.* **7**, 4000 (2014).
- ⁵T. Zhou, B. Lenoir, M. Colin, A. Dauscher, R. Al Rahal Al Orabi, P. Gougeon, M. Potel, and E. Guilmeau, *Appl. Phys. Lett.* **98**, 162106 (2011).
- ⁶P. Gougeon, P. Gall, R. Al Rahal Al Orabi, B. Fontaine, R. Gautier, M. Potel, T. Zhou, B. Lenoir, M. Colin, C. Candolfi, and A. Dauscher, *Chem. Mater.* **24**, 2899 (2012).
- ⁷R. Al Rahal Al Orabi, P. Gougeon, P. Gall, B. Fontaine, R. Gautier, M. Colin, C. Candolfi, A. Dauscher, J. Hejtmanek, B. Malaman, and B. Lenoir, *Inorg. Chem.* **53**, 11699 (2014).
- ⁸S. R. Brown, S. M. Kauzlarich, F. Gascoin, and G. J. Snyder, *Chem. Mater.* **18**, 1873 (2006).
- ⁹S. K. Bux, A. Zevalkink, O. Janka, D. Uhl, S. Kauzlarich, J. G. Snyder, and J.-P. Fleurial, *J. Mater. Chem. A* **2**, 215 (2014).
- ¹⁰K. Suekuni, F. S. Kim, H. Nishiate, M. Ohta, H. I. Tanaka, and T. Takabatake, *Appl. Phys. Lett.* **105**, 132107 (2014).
- ¹¹S. Ohno, U. Aydemir, M. Amsler, J.-H. Pöhl, S. Chanakian, A. Zevalkink, M. A. White, S. K. Bux, C. Wolverton, and G. J. Snyder, *Adv. Funct. Mater.* **27**, 1606361 (2017).
- ¹²U. Aydemir, A. Zevalkink, A. Ormeci, S. K. Bux, and G. J. Snyder, *J. Mater. Chem. A* **4**, 1867 (2016).
- ¹³G. S. Nolas, J. L. Cohn, G. A. Slack, and S. B. Schujman, *Appl. Phys. Lett.* **73**, 178 (1998).
- ¹⁴K. Suekuni, M. A. Avila, K. Umeo, and T. Takabatake, *Phys. Rev. B* **75**, 195210 (2007).
- ¹⁵M. A. Avila, K. Suekuni, K. Umeo, H. Fukuoka, S. Yamanaka, and T. Takabatake, *Phys. Rev. B* **74**, 125109 (2006).
- ¹⁶J. Fulmer, O. I. Lebedev, V. V. Roddatis, D. C. Kaseman, S. Sen, J.-A. Dolyniuk, K. Lee, A. V. Olenov, and K. Kovnir, *J. Am. Chem. Soc.* **135**, 12313 (2013).
- ¹⁷K. Suekuni, M. A. Avila, K. Umeo, H. Fukuoka, S. Yamanaka, T. Nakagawa, and T. Takabatake, *Phys. Rev. B* **77**, 235119 (2008).
- ¹⁸A. Bientien, M. Christensen, J. D. Bryan, A. Sanchez, S. Paschen, F. Steglich, G. D. Stucky, and B. B. Iversen, *Phys. Rev. B* **69**, 045107 (2004).
- ¹⁹F. Failamani, A. Grytsiv, G. Giester, G. Polt, P. Heinrich, H. Michor, E. Bauer, M. Zehetbauer, and P. Rogl, *Phys. Chem. Chem. Phys.* **17**, 24248 (2015).
- ²⁰D. J. Safarik, T. Klimczuk, A. Llobet, D. D. Byler, J. C. Lashley, J. R. O'Brien, and N. R. Dilley, *Phys. Rev. B* **85**, 014103 (2012).
- ²¹D. C. Schmitt, N. Haldolaarachchige, Y. Xiong, D. P. Young, R. Jin, and J. Y. Chan, *J. Am. Chem. Soc.* **134**, 5965 (2012).
- ²²T. Takabatake, K. Suekuni, T. Nakayama, and E. Kaneshita, *Rev. Mod. Phys.* **86**, 669 (2014).
- ²³M. Christensen, S. Johnsen, and B. B. Iversen, *Dalton Trans.* **39**, 978 (2010).
- ²⁴K. A. Kovnir and A. V. Shevelkov, *Russ. Chem. Rev.* **73**, 999 (2004).
- ²⁵T. Tadano, Y. Gohda, and S. Tsuneyuki, *Phys. Rev. Lett.* **104**, 095501 (2015).
- ²⁶H. Euchner, S. Pailhès, L. T. K. Nguyen, W. Assmus, F. Ritter, A. Haghighirad, Y. Grin, S. Paschen, and M. De Boissieu, *Phys. Rev. B* **86**, 224303 (2012).
- ²⁷M. S. Ikeda, H. Euchner, X. Pan, P. Tomes, A. Prokofiev, L. Prochaska, G. Lientschnig, R. Svagera, S. Hartmann, E. Gati, M. Lang, and S. Paschen, *Nat. Commun.* **10**, 887 (2019).
- ²⁸G. S. Nolas, J. L. Cohn, J. S. Dyck, C. Uher, and J. Yang, *Phys. Rev. B* **65**, 165201 (2002).
- ²⁹J. L. Cohn, G. S. Nolas, V. Fessatidis, T. H. Metcalf, and G. A. Slack, *Phys. Rev. Lett.* **82**, 779 (1999).
- ³⁰G. S. Nolas, T. J. R. Weakley, J. L. Cohn, and R. Sharma, *Phys. Rev. B* **61**, 3845 (2000).
- ³¹B. C. Sales, B. C. Chakoumakos, R. Jin, J. R. Thompson, and D. Mandrus, *Phys. Rev. B* **63**, 245113 (2001).
- ³²S. Paschen, W. Carrillo-Cabrera, A. Bientien, V. H. Tran, M. Baenitz, Y. Grin, and F. Steglich, *Phys. Rev. B* **64**, 214404 (2001).
- ³³B. C. Chakoumakos, B. C. Sales, and D. G. Mandrus, *J. Alloys Compd.* **322**, 127 (2001).
- ³⁴J. Xu, J. Tang, K. Sato, Y. Tanabe, H. Miyasaka, M. Yamashita, S. Heguri, and K. Tanigaki, *Phys. Rev. B* **82**, 085206 (2010).
- ³⁵P.-F. Lory, S. Pailhès, V. M. Giordano, H. Euchner, N. D. Nguyen, R. Ramlau, H. Borrmann, M. Schmidt, M. Baitinger, M. Ikeda, P. Tomes, M. Mihalkovic, C. Allio, M. R. Johnson, H. Schober, Y. Sidis, F. Bourdarot, L. P. Regnault, J. Ollivier, S. Paschen, Y. Grin, and M. de Boissieu, *Nat. Commun.* **8**, 491 (2017).
- ³⁶A. Ormeci and Y. Grin, *J. Thermoelectr.* **6**, 16 (2015).
- ³⁷Y. Grin, *J. Solid State Chem.* **73**, 1149 (2019).

- ³⁸H. Shimizu, T. Iitaka, T. Fukushima, T. Kume, S. Sasaki, N. Sata, Y. Ohishi, H. Fukuoka, and S. Yamanaka, *J. Appl. Phys.* **101**, 063549 (2007).
- ³⁹K. Suekuni, Y. Takasu, T. Hasegawa, N. Ogita, M. Udagawa, M. A. Avila, and T. Takabatake, *Phys. Rev. B* **81**, 205207 (2010).
- ⁴⁰R. Baumbach, F. Bridges, L. Downward, D. Cao, P. Chesler, and B. Sales, *Phys. Rev. B* **71**, 024202 (2005).
- ⁴¹A. N. Mansour, J. Martin, W. Wong-Ng, and G. S. Nolas, *J. Phys. Condens. Matter* **24**, 485503 (2012).
- ⁴²R. P. Hermann, W. Schweika, O. Leupold, R. Rüffer, G. S. Nolas, F. Grandjean, and G. J. Long, *Phys. Rev. B* **72**, 174301 (2005).
- ⁴³K. Umeo, M. A. Avila, T. Sakata, K. Suekuni, and T. Takabatake, *J. Phys. Soc. Jpn.* **74**, 2145 (2005).
- ⁴⁴I. Ishii, Y. Suetomi, T. K. Fujita, K. Suekuni, T. Tanaka, T. Takabatake, and T. Suzuki, *Phys. Rev. B* **85**, 085101 (2012).
- ⁴⁵T. Mori, K. Iwamoto, S. Kushibiki, H. Honda, H. Matsumoto, N. Toyota, M. A. Avila, K. Suekuni, and T. Takabatake, *Phys. Rev. Lett.* **106**, 015501 (2011).
- ⁴⁶A. Fujiwara, K. Sugimoto, C.-H. Shih, H. Tanaka, J. Tang, Y. Tanabe, J. Xu, S. Heguri, K. Tanigaki, and M. Takata, *Phys. Rev. B* **85**, 144305 (2012).
- ⁴⁷X. Zheng, S. Y. Rodriguez, and J. H. Ross Jr, *Phys. Rev. B* **84**, 024303 (2011).
- ⁴⁸K. Suekuni, S. Yamamoto, M. A. Avila, and T. Takabatake, *J. Phys. Soc. Jpn.* **77**, 61 (2008).
- ⁴⁹J. S. Tse, D. D. Klug, J. Y. Zhao, W. Sturhahn, E. E. Alp, J. Baumert, C. Gutt, M. R. Johnson, and W. Press, *Nat. Mater.* **4**, 917 (2005).
- ⁵⁰M. Christensen, A. B. Abrahamsen, N. B. Christensen, F. Juranyi, N. H. Andersen, K. Lefmann, J. Andreasson, C. R. H. Bahl, and B. B. Iversen, *Nat. Mater.* **7**, 811 (2008).
- ⁵¹M. M. Koza, M. R. Johnson, H. Mutka, M. Rotter, N. Nasir, A. Grytsiv, and P. Rogl, *Phys. Rev. B* **82**, 214301 (2010).
- ⁵²S. Johnsen, M. Christensen, B. Thomsen, G. K. H. Madsen, and B. B. Iversen, *Phys. Rev. B* **82**, 184303 (2010).
- ⁵³S. Pailhès, H. Euchner, V. M. Giordano, R. Debord, A. Assy, S. Gomès, A. Bosak, D. Machon, S. Paschen, and M. de Boissieu, *Phys. Rev. Lett.* **113**, 025506 (2014).
- ⁵⁴M. Christensen, S. Johnsen, F. Juranyi, and B. B. Iversen, *J. Appl. Phys.* **105**, 073508 (2009).
- ⁵⁵F. Dubois and T. F. Fässler, *J. Am. Chem. Soc.* **127**, 3264 (2005).
- ⁵⁶A. Kaltzoglou, S. D. Hoffmann, and T. F. Fässler, *Eur. J. Inorg. Chem.* **2007**, 4162 (2007).
- ⁵⁷A. Kaltzoglou, T. Fässler, M. Christensen, S. Johnsen, B. B. Iversen, I. Presniakov, A. Sobolev, and A. Shevelkov, *J. Mater. Chem.* **18**, 5630 (2008).
- ⁵⁸A. Kaltzoglou, T. F. Fässler, C. Goldb, E.-W. Scheidt, W. Scherer, T. Kume, and H. Shimizu, *J. Solid State Chem.* **182**, 2924 (2009).
- ⁵⁹M. Baitinger, B. Böhme, A. Ormeci, and Y. Grin, "Solid state chemistry of clathrate phases: Crystal structure, chemical bonding and preparation routes," in *The Physics and Chemistry of Inorganic Clathrates* (Springer, 2014), pp. 35–64.
- ⁶⁰S. Christensen, L. Bjerg, A. Kaltzoglou, F. Juranyi, T. Fässler, T. Unruh, and M. Christensen, *J. Appl. Phys.* **113**, 084902 (2013).
- ⁶¹K. Parlinski, see <http://wolf.ifj.edu.pl/phonon> for Software PHONON.
- ⁶²J. Hafner and M. Krajci, *J. Phys. Condens. Matter* **5**, 2489 (1993).
- ⁶³U. Aydemir, C. Candolfi, H. Borrmann, M. Baitinger, A. Ormeci, W. Carrillo-Cabrera, C. Chubilleau, B. Lenoir, A. Dauscher, N. Oeschler, F. Steglich, and Y. Grin, *Dalton Trans.* **39**, 1078 (2010).
- ⁶⁴W. Carrillo-Cabrera, M. Baitinger, B. Uslu, and Y. Grin, in *Materials Science*, edited by W. Grogger, F. Hofer, and P. Pötl (Verlag der TU Graz, 2009), Vol. 3, available at <http://www.computingformaterials.com>.
- ⁶⁵G. Squires, *Introduction to the Theory of Thermal Neutron Scattering* (Dover Publications, Inc., Mineola, New York, 1996).
- ⁶⁶M. M. Koza, L. Capogna, A. Leithe-Jasper, H. Rosner, W. Schnelle, H. Mutka, M. R. Johnson, C. Ritter, and Y. Grin, *Phys. Rev. B* **81**, 174302 (2010).
- ⁶⁷M. M. Koza, A. Leithe-Jasper, H. Rosner, W. Schnelle, H. Mutka, M. R. Johnson, M. Krisch, L. Capogna, and Y. Grin, *Phys. Rev. B* **84**, 014306 (2011).
- ⁶⁸M. M. Koza, A. Leithe-Jasper, H. Rosner, W. Schnelle, H. Mutka, M. R. Johnson, and Y. Grin, *Phys. Rev. B* **89**, 014302 (2014).
- ⁶⁹M. M. Koza, M. Boehm, E. Sischka, W. Schnelle, H. Mutka, and A. Leithe-Jasper, *Phys. Rev. B* **91**, 014305 (2015).
- ⁷⁰J. S. Tse, Z. Li, and K. Uehara, *Europhys. Lett.* **56**, 261 (2001).
- ⁷¹H. Shimizu, T. Imai, T. Kume, S. Sasaki, A. Kaltzoglou, and T. F. Fässler, *Chem. Phys. Lett.* **464**, 54 (2008).
- ⁷²T. Dahm and K. Ueda, *Phys. Rev. Lett.* **99**, 187003 (2007).
- ⁷³H. Mutka, M. M. Koza, M. R. Johnson, Z. Hiroi, J.-I. Yamaura, and Y. Nagao, *Phys. Rev. B* **78**, 104307 (2008).
- ⁷⁴M. M. Koza, A. Leithe-Jasper, E. Sischka, W. Schnelle, H. Borrmann, H. Mutka, and Y. Grin, *Phys. Chem. Chem. Phys.* **16**, 27119 (2014).
- ⁷⁵M. M. Koza, H. Mutka, Y. Okamoto, J.-I. Yamaura, and Z. Hiroi, *Phys. Chem. Chem. Phys.* **17**, 24837 (2015).
- ⁷⁶E. Shoko, G. J. Kearley, V. K. Peterson, H. Mutka, M. M. Koza, J.-I. Yamaura, Z. Hiroi, and G. J. Thorogood, *J. Phys. Condens. Matter* **26**, 305401 (2014).
- ⁷⁷U. Aydemir, C. Candolfi, A. Ormeci, Y. Oztan, M. Baitinger, N. Oeschler, F. Steglich, and Y. Grin, *Phys. Rev. B* **84**, 195137 (2011).
- ⁷⁸A. Bienten, E. Nishikori, S. Paschen, and B. B. Iversen, *Phys. Rev. B* **71**, 144107 (2005).
- ⁷⁹U. Aydemir, C. Candolfi, A. Ormeci, M. Baitinger, U. Burkhardt, N. Oeschler, F. Steglich, and Y. Grin, *Dalton Trans.* **44**, 7524 (2015).
- ⁸⁰U. Aydemir, C. Candolfi, A. Ormeci, M. Baitinger, N. Oeschler, F. Steglich, and Y. Grin, *J. Phys. Condens. Matter* **26**, 485801 (2014).
- ⁸¹C. Candolfi, U. Aydemir, M. M. Koza, M. Baitinger, Y. Grin, and F. Steglich, *J. Phys. Condens. Matter* **27**, 485401 (2015).
- ⁸²C. Candolfi, U. Aydemir, M. Baitinger, N. Oeschler, F. Steglich, and Y. Grin, *J. Appl. Phys.* **111**, 043706 (2012).